Integrative experimental/computational approach establishes active cellular protrusion as the primary driving force of phagocytic spreading by immune cells

Short Title: Computational modeling of immune cell spreading

Emmet A. Francis[1*], Volkmar Heinrich[1*]

[1] Department of Biomedical Engineering, University of California Davis, Davis, CA, USA

* Corresponding author

E-mail: eafrancis@ucdavis.edu (EAF), vheinrich@ucdavis.edu (VH)

Abstract

The dynamic interplay between cell adhesion and protrusion is a critical determinant of many forms of cell motility. When modeling cell spreading on adhesive surfaces, traditional mathematical treatments often consider passive cell adhesion as the primary, if not exclusive, mechanistic driving force of this cellular motion. To better assess the contribution of active cytoskeletal protrusion to immune-cell spreading during phagocytosis, we here develop a computational framework that allows us to optionally investigate both purely adhesive spreading ("Brownian zipper hypothesis") as well as protrusion-dominated spreading ("protrusive zipper hypothesis"). We model the cell as an axisymmetric body of highly viscous fluid surrounded by a cortex with uniform surface tension and incorporate as potential driving forces of cell spreading an attractive stress due to receptor-ligand binding and an outward normal stress representing cytoskeletal protrusion, both acting on the cell boundary. We leverage various model predictions against the results of a directly related experimental companion study of human neutrophil phagocytic spreading on substrates coated with different densities of antibodies. We find that the concept of adhesion-driven spreading is incompatible with experimental results such as the independence of the cell-spreading speed on the density of immobilized antibodies. In contrast, the protrusive zipper model agrees well with experimental findings and, when adapted to simulate cell spreading on discrete adhesion sites, it also reproduces the observed positive correlation between antibody density and maximum cell-substrate contact area. Together, our integrative experimental/computational approach shows that phagocytic spreading is driven by cellular protrusion, and that the extent of spreading is limited by the density of adhesion sites.

Author Summary

To accomplish many routine biological tasks, cells must rapidly spread over different types of surfaces. Here, we examine the biophysical underpinnings of immune cell spreading during phagocytosis, the process by which white blood cells such as neutrophils engulf pathogens or other foreign objects. Our computational framework models the case in which a human neutrophil spreads over a flat surface coated with antibodies, which we also test experimentally in a companion paper. Our primary purpose is to assess whether phagocytic spreading is actively driven by protrusive forces exerted by the cell, or passively by adhesive forces acting between receptors in the cell membrane and antibodies on the surface. By directly comparing our model predictions to experimental results, we demonstrate that phagocytic spreading is primarily driven by protrusion, but the extent of spreading is still limited by the availability of binding sites. Our findings improve the fundamental understanding of phagocytosis and may also pave the way for future investigations of the balance between adhesion and protrusion in other forms of cell spreading, such as wound healing or cancer cell migration.

Introduction

The ability of cells to spread on surfaces is critical to many biological processes, including cell migration, wound healing, and tissue formation. Immune cells are especially adept at rapid spreading; for instance, neutrophils commonly travel up to an order of magnitude faster in motility assays than fibroblasts or endothelial cells [1-5]. Vital immune cell functions, such as firm arrest at the endothelium and phagocytosis of pathogens, rely on this ability. A deeper understanding of the physical mechanisms driving cell spreading is essential for informed pharmaceutical strategies and new therapies targeting immune cells, such as current efforts to enhance phagocytosis for more effective clearance of cancer cells [6, 7].

Many experimental and theoretical studies have sought to unravel the physical principles of cell spreading by analyzing the initial growth of cell contact regions on a flat, adhesive substrate [8-11]. However, it often remains unclear whether any given type of cell spreading is primarily driven by passive forces due to adhesion or by active protrusive and/or contractile forces generated by the cell. In the simplest model, cell spreading is treated as a purely passive process, similar to a viscous droplet spreading on an adhesive substrate [8, 12, 13]. Alternative models assume that cytoskeleton-driven protrusion determines the rate of cell spreading, neglecting the effective attractive pre-contact force due to ligand-receptor interactions [10, 14, 15].

Here, we aim to illuminate fundamental cell-spreading mechanisms by focusing on the mechanistic driving force of phagocytic spreading. In conventional phagocytosis, an immune cell first adheres to the surface of a target particle such as a bacterium, often by binding to opsonic ligands such as immunoglobulin G (IgG) antibodies. The cell then spreads over the target surface

83 until its membrane closes around the particle. On the other hand, when presented with an
84 excessively large target, the cell is unable to fully engulf the particle and continues to spread
85 until its target-contact area reaches a maximum [16, 17]. Such cases, including phagocytic
86 spreading on flat substrates, are termed frustrated phagocytosis. The relatively simple geometry
87 of a cell undergoing frustrated phagocytic spreading on a flat surface is particularly amenable to
88 theoretical analysis, especially when the cell spreads in an axisymmetric manner. Moreover, it
89 seems reasonable to assume that some of the insights generated by integrative
90 experimental/theoretical analyses of cell spreading on flat surfaces also carry over to other
91 geometries [18-21]. For example, a previous mathematical model of phagocytosis has been able
92 to predict experimentally observed variations in the engulfment of spherical particles in the size
93 range of 3-11μm by changing only one model parameter value, i.e., the input size of the target
94 bead [22].

95 Reflecting the above-mentioned contrasting mechanistic notions about the driving force
96 of generic cell spreading, two hypotheses have been put forward to explain phagocytic
97 spreading, i.e., the "Brownian zipper" and "protrusive zipper" models [23]. Both models concur
98 that fresh contact between the cell membrane and target surface results in a zipper-like adhesive
99 attachment that is essentially irreversible, in agreement with experimental observations [16, 24,
100 25]. However, regarding the driving force of cellular advancement, the Brownian zipper model
101 postulates that strong adhesion alone is responsible for pulling the cell membrane onto the target
102 surface. In contrast, the protrusive zipper model assumes that an active protrusive force
103 generated by the cytoskeleton is the predominant driver of outward motion of the cell surface,
104 without excluding a possible contribution of adhesive cell-substrate interactions. It is important
105 to bear in mind that our definition of these two models in terms of the driving force of spreading

106 is not the same as the distinction between “passive” and “active zippers” used elsewhere [26]. In
107 contrast, neither of the zipper models defined in [26] included an active protrusive force in the
108 computations but instead implemented an effective adhesion stress as the sole driving force of
109 spreading. Therefore, both zipper models defined in [26] fall into the category of a Brownian
110 zipper as defined here.

111 We seek to establish which of these hypotheses is more realistic by developing
112 mathematical models of the mechanics of isotropic cell spreading and comparing our theoretical
113 predictions with experimental observations of human neutrophils spreading on flat, IgG-coated
114 surfaces. As reported in detail in a companion paper, our experimental design allowed us to
115 examine the spreading behavior of neutrophils on surfaces coated with different densities of IgG
116 [24]. Because higher IgG densities correspond to stronger adhesive forces, we reasoned that the
117 Brownian zipper model should predict a much stronger correlation between IgG density and rate
118 of contact-area growth (“spreading speed”) than the protrusive zipper model. Here, we use
119 computer simulations of phagocytic spreading to verify this common-sense expectation and
120 further investigate mechanisms governing immune-cell spreading. First, we present the
121 predictions of a Brownian zipper model that realistically implements known insights about the
122 mechanical behavior of human neutrophils. Then, we investigate the protrusive zipper model,
123 including the contribution of adhesive pre-contact interactions to the driving force of spreading.
124 Finally, we also present a version of the Brownian zipper model that implements the discrete
125 nature of receptor-ligand interactions more realistically than the continuum models introduced
126 earlier. Together, our integrative experimental/theoretical approach establishes that the Brownian
127 zipper model is inconsistent with experimental results, whereas the spreading dynamics predicted
128 by the protrusive zipper model agree well with our experiments.

Results

Model implementation of key biophysical mechanisms of cell spreading

We consider a simple model cell that captures the basic geometrical and mechanical properties of human neutrophils, the most abundant type of white blood cell and one of the prototypes of professional phagocytes. This model cell consists of an axisymmetric, highly viscous fluid body of constant volume that is surrounded by an elastic cortex with uniform tension (Fig 1). Termed the "cortical shell, liquid core model", this theoretical concept has successfully reproduced the passive response of human neutrophils to imposed deformations [27, 28]. In the undeformed reference state, the persistent tension of the cortex maintains a spherical cell shape with a typical diameter of 8.5 μm. The nucleus of neutrophils is segmented into two to five lobes [29, 30] and appears to play only a minor role during deformations, lending support to the approximation of the cell interior as a homogeneous fluid. The effective viscosity (μ) of the cytoplasm has been found to be about 200,000 times the viscosity of water at room temperature in passive neutrophils [27, 28], and another ~3-times higher in active neutrophils [31]. It is well known to increase during phagocytosis [22, 32, 33]. We use a viscosity value of μ = 200 Pa-s in our passive Brownian zipper model and a value of μ = 1660 Pa-s in our active protrusive zipper model. The original assumption of a constant cortical tension [27] was later found to be approximately true only for small deformations [34]. The revised relationship between tension (τ) and cell surface area (A_{cell}) was shown to be roughly biphasic [35]. Assuming an isotropic and

uniform tension, our simulations incorporate a smoothed version of the following biphasic constitutive relationship, in overall agreement with a number of quantitative experimental studies [22, 35, 36] (plotted in S6 Appendices, Appendix C):

$$\tau(A_{cell}) = \begin{cases} 0.01 + 0.16\left(\dfrac{A_{cell}}{A_{cell,0}} - 1\right)\dfrac{\mathrm{mN}}{\mathrm{m}} & \text{if} \quad \dfrac{A_{cell}}{A_{cell,0}} \le 1.26 \\ 0.0516 + 0.545\left(\dfrac{A_{cell}}{A_{cell,0}} - 1.26\right)\dfrac{\mathrm{mN}}{\mathrm{m}} & \text{if} \quad \dfrac{A_{cell}}{A_{cell,0}} > 1.26 \end{cases} \tag{1}$$

where $A_{cell,0}$ is the surface area of the resting neutrophil before spreading. We also tested alternative versions of this constitutive relationship in S6 Appendices, Appendix C, and found that they do not qualitatively alter the results of our simulations.

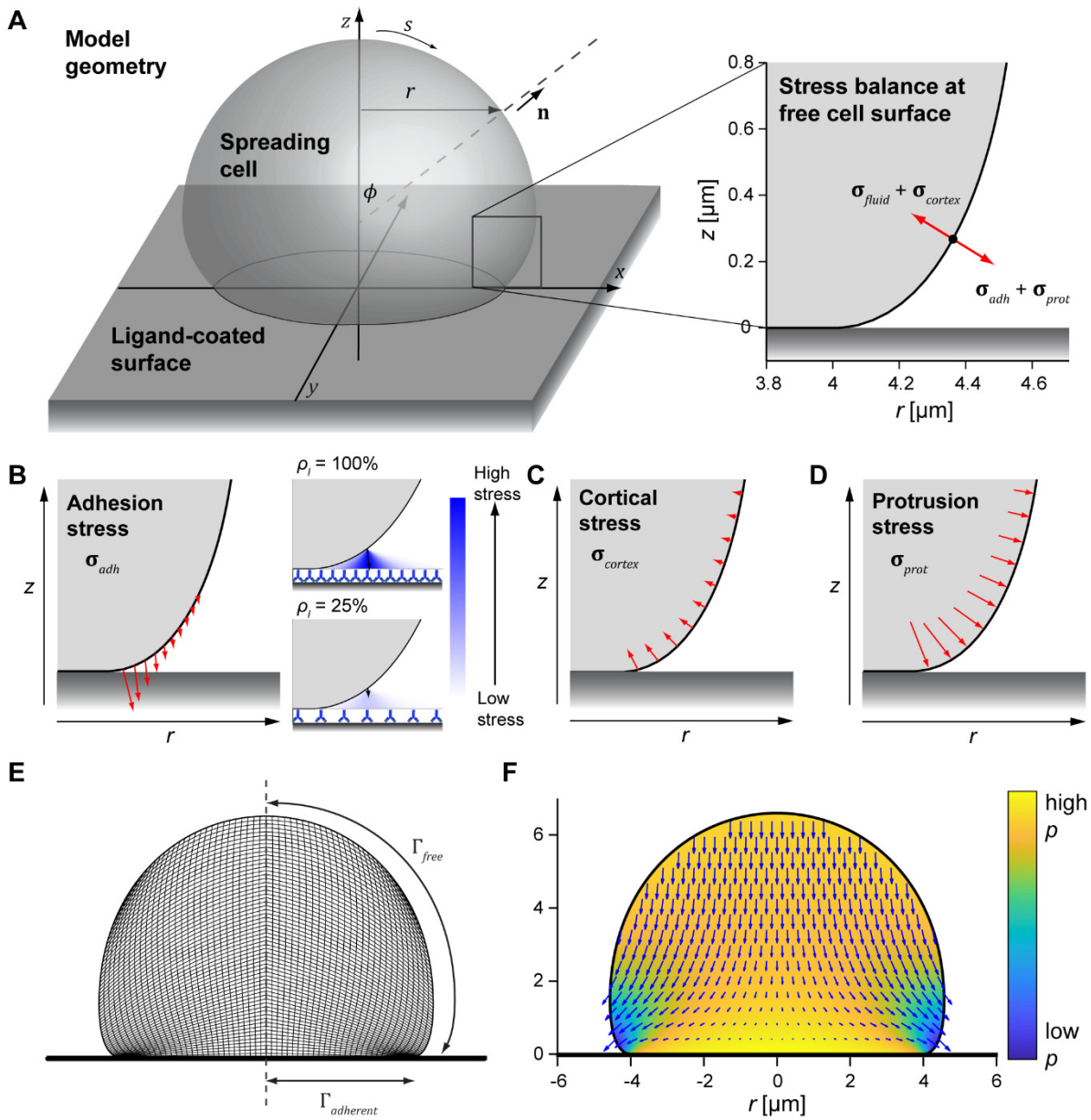

Fig 1. Illustration of our computational model of isotropic cell spreading. (A) 3D rendering shows the geometry and defines coordinates for an axisymmetric spreading cell on a flat surface. The enlarged inset (right) illustrates the stress balance at the free cell boundary. (B) Pre-contact adhesion stress effectively pulls the membrane onto the flat surface. The enlarged insets conceptually depict how the adhesion stress is computed for different ligand densities ρ_l. (C) Cortical tension and membrane curvature give rise to an effective inward normal stress. (D) The protrusion stress acts normal to the cell membrane and is concentrated at the region of the membrane closest to the substrate. (E) The cross-sectional snapshot of a simulation illustrates the mesh composed of quadrilateral elements used in the calculations, with tighter element packing closer to the flat surface. The computational domain only includes half

of this mesh due to axial symmetry. Boundary regions are labeled Γ, and the vertical dashed line is the symmetry axis ($r = 0$) (F) This snapshot of a simulation illustrates the fluid velocity (vector field) and relative pressure (heat map) computed for a given cell shape with known boundary stresses.

Movements of the viscous cytoplasm generally do not exceed velocities of 1 μm/s during phagocytic cell spreading and are characterized by low Reynolds numbers. Such movements are well described by the Stokes equations for creeping flow:

$$\mu \nabla^2 \mathbf{v} = \nabla p \tag{2}$$

along with the continuity equation for incompressible fluids:

$$\nabla \cdot \mathbf{v} = 0 \tag{3}$$

Here, $\mathbf{v}$ denotes the fluid velocity vector, and p is fluid pressure. Together, these equations govern the flow behavior of our model cell.

Interactions between the cell surface and the substrate can facilitate cell spreading directly via adhesion, and indirectly through receptor-induced signaling that leads to protrusion. Including the respective stresses, the moving boundary condition governing the free (i.e., nonadherent) part of the cell surface (Γ_{free}) balances up to four types of stress vectors: fluid stress ($\boldsymbol{\sigma}_{fluid}$), adhesion stress ($\boldsymbol{\sigma}_{adh}$), protrusion stress ($\boldsymbol{\sigma}_{prot}$), and cortical stress ($\boldsymbol{\sigma}_{cortex}$) (Fig 1A):

$$\boldsymbol{\sigma}_{fluid} + \boldsymbol{\sigma}_{adh} + \boldsymbol{\sigma}_{cortex} + \boldsymbol{\sigma}_{prot} = \mathbf{0} \quad \text{on } \Gamma_{free} \tag{4}$$

The fluid stress vector $\boldsymbol{\sigma}_{fluid}$ encompasses the pressure difference across the cell surface as well as the stress exerted on the surface by the moving cytoplasm. It is determined by the constitutive relation for a Newtonian fluid:

$$\boldsymbol{\sigma}_{fluid} = \boldsymbol{\sigma}_{fluid,out} - \boldsymbol{\sigma}_{fluid,in} = (p - p_{out})\mathbf{n} - \mu\left(\nabla \mathbf{v} + (\nabla \mathbf{v})^T\right) \cdot \mathbf{n} \tag{5}$$

where $\mathbf{n}$ is the unit surface normal, and the dot in the last term on the right-hand side denotes the inner product between a tensor and a vector. The extracellular medium has a much lower viscosity than the intracellular fluid; therefore, Eq (5) neglects the medium's viscous contribution and only accounts for its hydrostatic pressure denoted p_{out}.

Our implementation of the adhesion stress is based on the assumption that adhesion can effectively be represented by a short-range attractive potential between the cell surface and the ligand-coated substrate. We compute the effective adhesion stress at a given point on the cell surface by summing over all pairwise interactions with substrate molecules that lie outside the cell-substrate contact region at the time (Fig 1B). For a continuum of ligand molecules, the resulting expression takes the form (derived in S6 Appendices, Appendix A)

$$\boldsymbol{\sigma}_{adh} = \sigma_o \rho_l \iint_{\text{substrate}} \mathbf{f}_{unit} \left[\left(\frac{D_0}{D} \right)^7 - \left(\frac{D_0}{D} \right)^4 \right] dA \tag{6}$$

where ρ_l is the ligand surface density and σ_0 is a scaling factor representing the strength of interaction per unit area of the cell surface. The unit vector $\mathbf{f}_{unit}$ specifies the direction of a given interaction, D denotes the distance between the interacting points, and D_0 is a constant setting the overall range of the adhesion potential (set to 50 nm in our simulations; S7 Table).

The origin of the cortical stress is the cortical tension, which resists expansion of the cell surface area and acts along the curved surface of the cell (Fig 1D). The resulting stress acts normal to the surface and is given by the product of the tension τ (Eq (1)) and the mean curvature of the cell surface, as dictated by Laplace's law:

$$\boldsymbol{\sigma}_{cortex} = -\tau \left(\frac{\partial \phi}{\partial s} + \frac{\sin \phi}{r} \right) \mathbf{n} \tag{7}$$

211 Here, the term in parentheses is the mean curvature of the axisymmetric cell surface expressed in
212 the coordinates defined in Fig 1A.

213 The protrusion stress comprises outward forces exerted on the cell surface by the actively
214 remodeling cytoskeleton. Purposeful reorganization of intracellular structures requires tight
215 coordination by biochemical signaling cues, which in turn are induced by receptor-ligand
216 binding. Rather than attempting to implement these highly complex mechano-chemical
217 mechanisms, we capture their localized character in a semiempirical manner. Our model
218 postulates that the protrusive stress is greatest at the perimeter of the cell-substrate contact region
219 and decays as a function of the distance from this leading edge measured along the arc length (s,
220 Fig 1A) of the contour of the unbound cell surface. We assume that this stress acts normal to the
221 cell boundary, and that its decay along the free cell surface is exponential (Fig 1C):

222 $$\boldsymbol{\sigma}_{prot} = \sigma_{prot} e^{-\frac{s_{contact} - s}{s_0}} \mathbf{n} \tag{8}$$

223 In this equation, $s_{contact}$ is the arc length value at which the cell-surface contour makes contact
224 with the substrate, and s_0 is the characteristic length that sets the spatial range of the protrusion
225 stress.

226 Bearing in mind that cytoskeletal remodeling also is responsible for the behavior of the
227 cortical tension, and that the tension varies during cell spreading (Eq (1)), it is reasonable to
228 assume that the overall strength of the protrusion stress (σ_{prot}) varies in a similar fashion. In
229 addition to the spatial distribution of the cortical stress governed by Eq (8), we therefore also
230 postulate a deformation-dependent strength of the protrusive stress. Our choice of this
231 dependence, and its motivation, will be explained in a later section.

232 Finally, for the part of the cell surface that is in contact with the substrate, we enforce a
233 no-slip boundary condition, requiring that

234 $$\mathbf{v} = \mathbf{0} \quad \text{on } \Gamma_{adherent} \tag{9}$$

235 Each simulation begins with a model cell that rests on the surface and has formed a very
236 small initial contact footprint (area < 0.1 μm^2). The shape of the upper, free part of the cell at this
237 time is a spherical cap. We determine the fluid velocities and pressure distribution at each time
238 step by solving a perturbed form of the Stokes equations using the finite element method (FEM;
239 Fig 1E,F) as described previously [37]. We then use the computed velocities to evolve the cell
240 shape over a small time step. Details of our model implementation and solution method are given
241 in Methods and S6 Appendices, Appendix D.

242 This generic modeling framework of cell spreading can easily be adopted to represent
243 different mechanistic notions by adjusting the relative contributions of the adhesion and
244 protrusion stresses. Disregarding the protrusion stress altogether results in a mathematical
245 representation of the Brownian zipper model described in the Introduction. On the other hand,
246 the protrusive zipper model generally includes both the protrusion stress as well as the adhesion
247 stress. A purely protrusion-driven mode of spreading also can be tested by setting the pre-contact
248 adhesion stress to zero, although one needs to bear in mind that irreversible adhesion still
249 maintains the cell-substrate contact region in this case. In all model versions, the adhesion stress
250 can be varied over several orders of magnitude to predict how the spreading behavior depends on
251 the density of ligand displayed on the substrate.

252

253 # Quantitative experimental results for the validation of model
254 versions

255 The computational framework presented in the previous section can be adopted to
256 simulate interactions by various cell types with targets of different axisymmetric geometries. Our
257 present focus on human neutrophils spreading on flat substrates is motivated by a wealth of
258 experimental results obtained for this particular scenario and presented in a companion paper
259 [24]. In brief, we exposed cells to glass coverslips coated with IgG antibodies at densities (ρ_{IgG})
260 spanning ~3 orders of magnitude. The analysis of these highly controlled experiments included
261 measurements of the cell-substrate contact area of spreading cells over time (Fig 2). Regardless
262 of IgG density, we found that the area-versus-time curves typically were sigmoidal in shape (Fig
263 2B,C). Defining a cell's "spreading speed" as the fastest rate of contact-area growth (i.e., the
264 slope of a sigmoidal fit to the area-versus-time curve at the inflection point), we found that all
265 spreading cells increased their substrate-contact area at speeds of around 3 $\mu m^2/s$ irrespective of
266 the density of deposited IgG (Fig. 2D). The measured values of the maximum contact area of
267 spreading cells, on the other hand, exhibited a moderate but significant increase at higher IgG
268 densities (Fig 2E). These experimental results provide useful quantitative benchmarks for
269 comparison with computer simulations and will be used in the following sections to evaluate the
270 validity of different mechanistic notions about cell spreading.

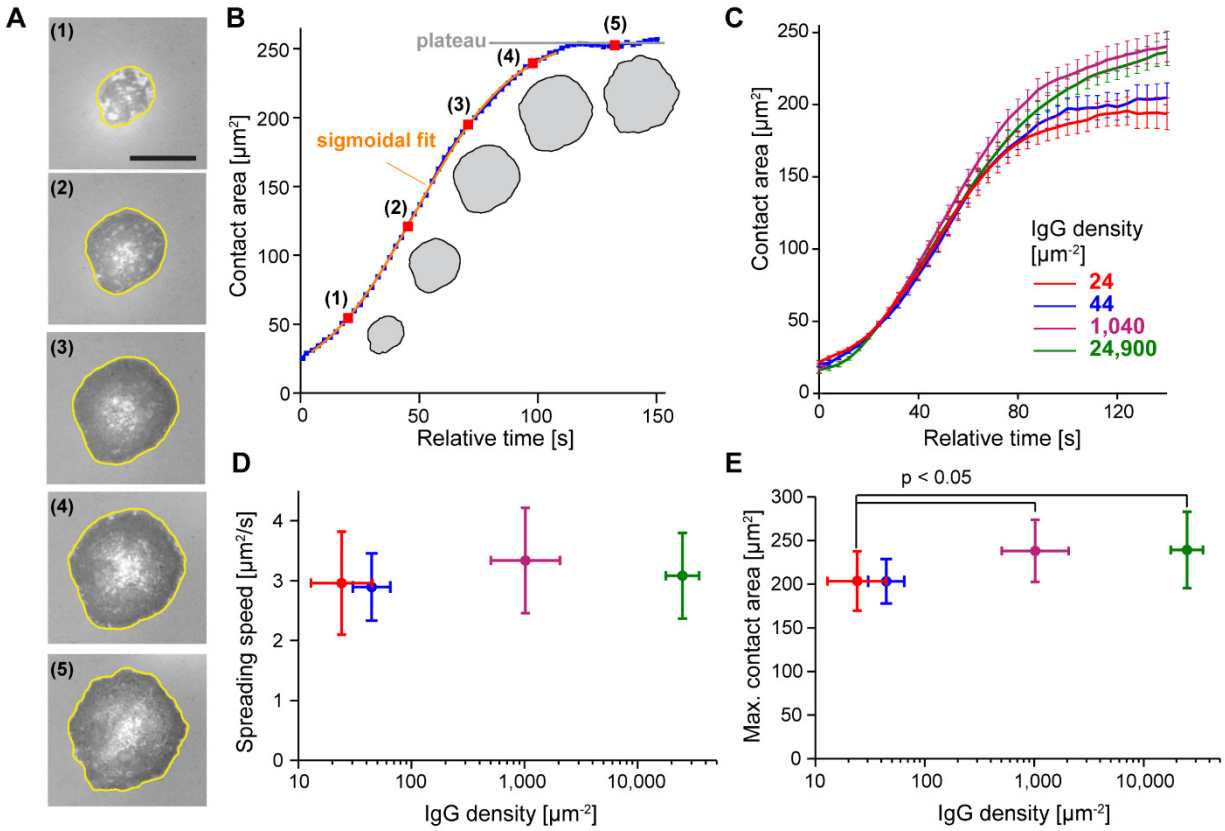

Fig 2. Summary of experimental results.
(A) The contact region of a spreading neutrophil was imaged using reflection interference contrast microscopy (RICM). Contact regions in this example are traced in yellow. The scale bar in the first image denotes 10 μm. (B) Contact area is plotted as a function of time for the spreading cell shown in (A). The spreading speed is defined as the maximum slope extracted from a sigmoidal fit, and the maximum contact area is given by averaging the contact area at the plateau. (C) Mean contact area is computed at discrete time values for aligned curves of cells spreading on different densities of IgG. Mean quantified IgG densities are reported in the figure legend as IgG molecules per μm^2. Error bars represent standard error of the mean. (D) Average spreading speed was quantified for the different IgG densities. There is no significant difference between mean slope values. (E) Maximum contact area increases slightly as a function of IgG density. Statistically significant differences in maximum contact area values were verified using ANOVA followed by a Tukey post hoc test. Error bars in both (D) and (E) indicate standard deviation. The IgG density was quantified for each condition as described in [24].

An additional measure of interest can be inferred from the actual surface densities of IgG used in the experiments. The most densely coated coverslips presented about 25,000 IgG

289 molecules per μm^2 and induced ~85% of deposited cells to spread. Remarkably, even at a low
290 IgG surface density of ~44 molecules per μm^2, about 30% of the deposited cells still spread in an
291 IgG-dependent manner. Fcγ receptors bind IgG with an average equilibrium constant of about
292 10^{-6} M [38], corresponding to a binding energy per bond of $E_{bind} = -k_B T \ln\left(10^{-6}\right) \approx 14 k_B T$.
293 Assuming that all IgG molecules in the cell-substrate contact region have formed bonds with the
294 cell's Fcγ receptors, conservative (upper-limit) estimates of the adhesion energy density of cell-
295 substrate interactions on substrates coated with the high and low numbers of IgG yield 1,500
296 μJ/m^2 and 2.6 μJ/m^2, respectively.

297

298 Purely adhesion-driven spreading: predictions by the Brownian 299 zipper model

300 We first tested the simplest version of our framework, the Brownian zipper model, by
301 simulating purely adhesion-driven spreading in the absence of any protrusion stress (Fig 3, S1
302 Movie). In this scenario, the model cell is passive and is pulled onto the substrate by short-range
303 attraction. This case is conceptually equivalent to a viscous droplet spreading on an adhesive
304 substrate.

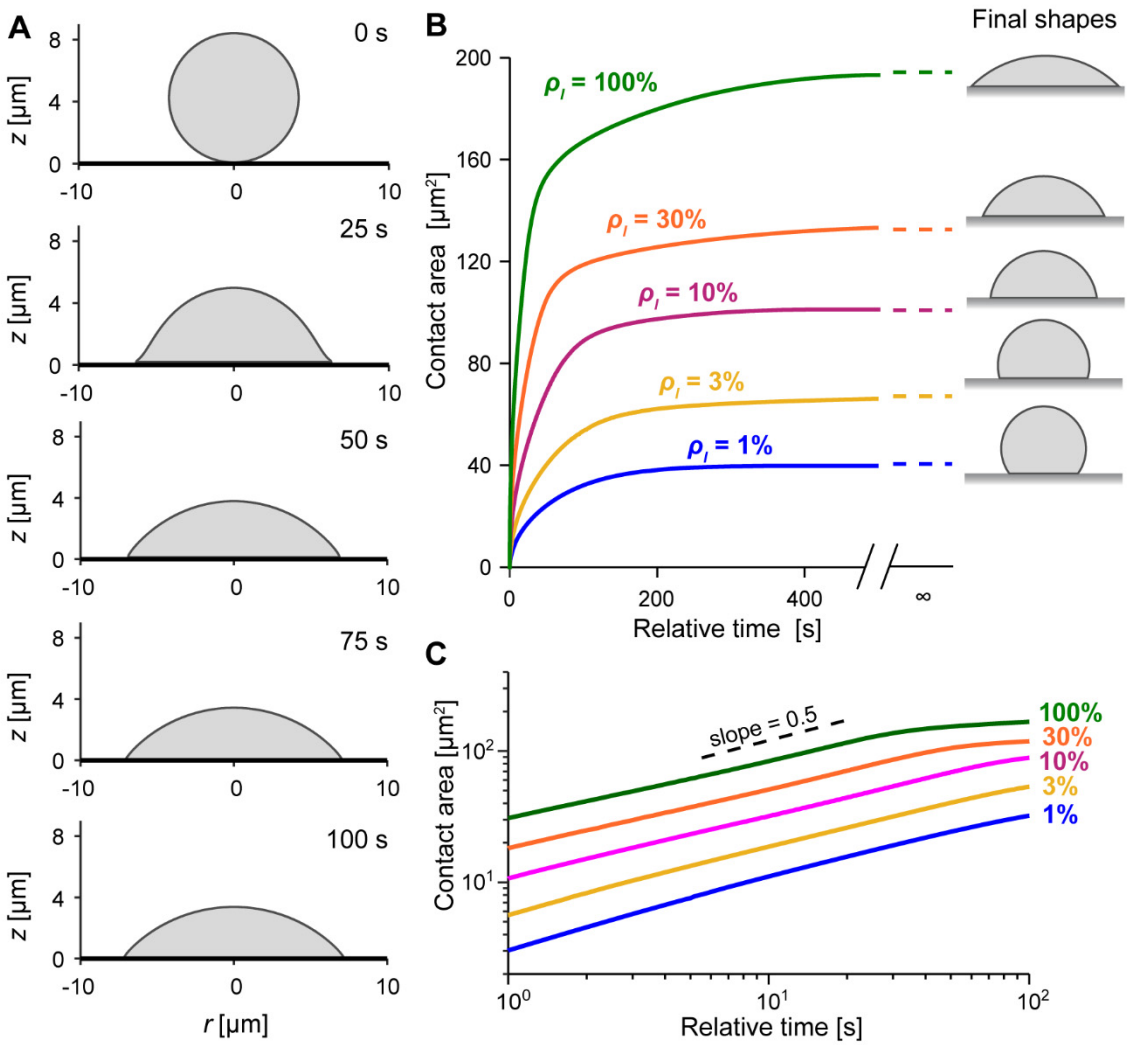

305

306 **Fig 3. Predictions of the Brownian zipper model.**
307 (A) A model cell spreading on the highest tested ligand density (100%) quickly approaches a
308 spherical cap morphology. Time stamps are included for each snapshot. (B) Curves of contact
309 area vs. time show that the spreading rate decreases monotonically. The contact area ultimately
310 approaches steady-state values predicted by the Young-Dupre equation (dashed lines). Predicted
311 equilibrium shapes are included on the right. (C) Log-log plot of contact area vs. time is nearly
312 linear over the initial spreading phase. The slope of this line corresponds to the exponent of a
313 power law describing contact area growth as a function of time. The dashed line shows a slope of
314 0.5 for reference.

315

316 Varying the ligand density ρ_l over two orders of magnitude, we found that the model

317 cells generally spread fastest immediately after first contacting the substrate. Afterwards, the

growth rate of the cell-substrate contact area decreased monotonically until the contact area reached a steady-state plateau marking equilibrium (Fig 3B). As expected, the equilibrium shapes were spherical caps. Log-log plots of the contact-area-versus-time predictions during the initial, fast spreading phase were approximately linear, with slopes close to 0.5 (Fig 3C). Hence, the contact-area growth initially obeys a power law, in agreement with various laws proposed to describe droplet wetting dynamics [39] or passive cell spreading [8, 13]. In fact, the exponent of 0.5 is an excellent match to results of a previous study that modeled cells as highly viscous droplets [13]. In S6 Appendices, Appendix B, we show how this exponent naturally arises during early spreading of a passive model cell driven by adhesion stresses concentrated at the contact perimeter.

Although the predictions of the Brownian zipper model agree well with the typical theoretical behavior expected for this kind of passive model cell, they clearly differ from the results of our phagocytic spreading experiments (Fig 2) in several important ways. First, the simulated contact-area-versus-time curves lack the characteristic sigmoidal shapes observed in experiments. Second, the predicted spreading curves exhibit a very strong dependence on the density of encountered ligands, in stark contrast to the observed spreading behavior. This dependence is evident in both the predicted spreading speeds, which increase dramatically with ligand density, as well as the predicted maximum contact areas, which increase several-fold as a function of the tested adhesive strengths.

Finally, the equilibrium shapes obtained for the adhesion energy densities used in the simulations are inconsistent with the cell deformations observed on the experimentally tested IgG densities. At equilibrium, the adhesion energy density (γ) of the Brownian zipper model cell is related to the cortical tension τ and the contact angle θ_c via the Young-Dupre equation:

$$\gamma = \tau(1 - \cos\theta_c) \tag{10}$$

For a given value of the maximum cell-substrate contact area A_c, the equilibrium shape of the model cell—a spherical cap—is uniquely defined by A_c and the known, constant cell volume. Thus, basic geometry allows us to calculate the contact angle θ_c as well as the total cell surface area A_{cell}. Inserting the value of the latter into Eq (1) provides the cortical tension at equilibrium, which then can be used in Eq (10) to obtain the adhesion energy density as a function of A_c (Fig 4). As expected, the relationship between maximum contact area and adhesion strength predicted by our numerical simulations agrees well with the Young-Dupre equation (S6 Appendices, Appendix A). The quantitative comparison of this theoretical prediction to actual adhesion energy densities—estimated from the densities of deposited IgG molecules as explained earlier—exposes entirely different behaviors between the model and experiments, however (Fig 4). Especially in experiments performed at lower IgG densities, the conservatively estimated adhesion energy densities were much lower than what would be required to form the measured maximum contact areas solely by adhesion. In summary, the results of this section rule out adhesion as the primary driving force of frustrated phagocytic spreading.

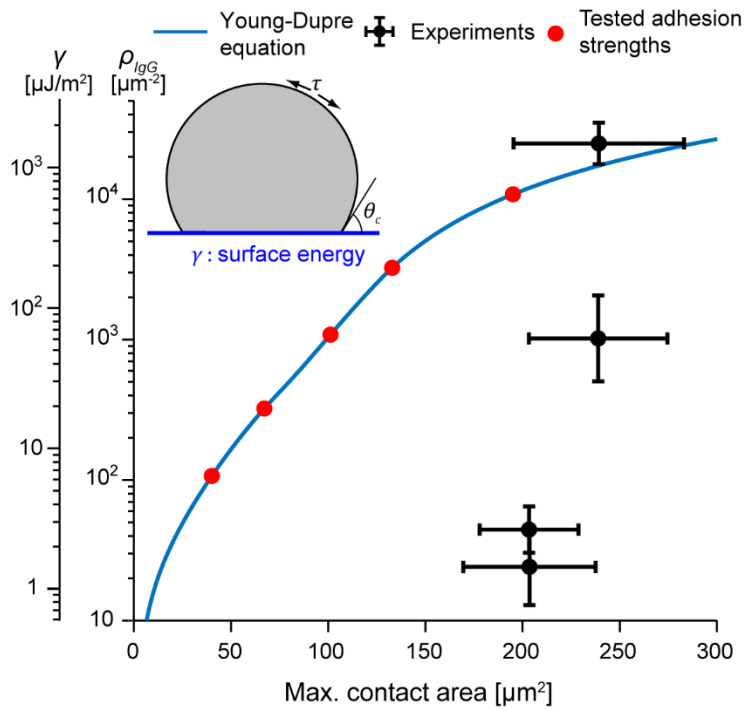

Fig 4. Relationship between ligand density and maximum contact area, as predicted by the Young-Dupre equation.
The adhesion energy γ, and therefore the ligand density ρ_{IgG}, can be expressed as a function of the contact area of the final spherical cap formed by a viscous droplet. The tested adhesion strengths are marked as red dots. Actual experimental values are shown for comparison. Error bars indicate standard deviation.

Protrusion-dominated spreading: predictions of the protrusive zipper model

The protrusive zipper model incorporates the protrusion stress into the basic framework considered in the previous section, enabling us to account for active force generation by the model cell. Our semiempirical implementation is motivated by biological plausibility, and by the goal to reproduce experimental observations with a minimum set of rules for the spatial distribution (Eq (8)) and the deformation-dependent evolution of the protrusion stress during cell

371 spreading. To capture the presumed correlation between receptor-induced signaling and
372 protrusive force generation by the cytoskeleton, we express the strength of the protrusion stress
373 as a function of the cell-substrate contact area A_c. We assume that in the initial low-tension
374 regime, the protrusion stress grows linearly with A_c. Once the cortical tension increases more
375 steeply, the protrusion stress is assumed to grow faster as well. Ultimately, the strength of the
376 protrusion stress levels out at a maximum value of $\sigma_{prot,max} = 3.5$ kPa, within the range of
377 experimentally measured stresses exerted by parallel actin filaments [40, 41]. This behavior is
378 implemented in our model through a smoothed version of the following rule (plotted in S6
379 Appendices, Appendix C):

380
$$\sigma_{prot} = \sigma_{prot,max} \times \begin{cases} \left[0.05 + 0.3\left(\dfrac{A_c}{A_{c,trans}}\right)\right] & \text{if} \quad \dfrac{A_{cell}}{A_{cell,0}} \le 1.26 \\ \left[0.35 + 0.65\left(\dfrac{A_c - A_{c,trans}}{120\ \mu\text{m}^2}\right)^{1/2}\right] & \text{if} \quad \dfrac{A_{cell}}{A_{cell,0}} > 1.26 \text{ and } A_c \le A_{c,trans} + 120\,\mu\text{m}^2 \\ 1 & \text{if} \quad A_c > A_{c,trans} + 120\,\mu\text{m}^2 \end{cases} \quad (11)$$

381 where $A_{c,trans}$ is the contact area when the total cell surface area A_{cell} is equal to $1.26A_{cell,0}$, the
382 transitional moment when the cortical tension starts rising more rapidly (Eq (1)).

383 We started examining the behavior of this model by first disregarding the adhesion stress
384 altogether. In this limiting scenario, cell spreading is driven by protrusion, whereas the only
385 remaining role of adhesion is to render cell-substrate contacts irreversible, as in all our models.
386 As mentioned above, cell-substrate contact is coupled to protrusion through biochemical
387 signaling via Eq 11. We found that in this case, the model cell begins spreading slowly while a
388 distinctive leading edge gradually develops (Fig 5A, S2 Movie), resulting in a morphology that
389 clearly differs from the spherical caps predicted by the Brownian zipper model (Fig 3).

Spreading slows noticeably at about 90 s, around the time the protrusion stress reaches its maximum value. The resulting contact-area-versus-time curve has a sigmoidal shape, in agreement with the mean spreading behavior observed in experiments on the highest density of IgG (Fig 5B). We also tested slightly different versions of Eq 11 and found that the overall curve remains sigmoidal even for these alternative relationships (S6 Appendices, Appendix C). On average, spreading appears to commence somewhat more gradually in experiments than in our model, which may indicate an overestimate of the initial protrusion stress in Eq 11. Plots of the protrusion stress and the cortical tension as a function of time (Fig 5C) illustrate the qualitatively similar evolution of these two quantities, with the rise of the tension lagging due to the initial "slack" of the cell surface in the low-tension regime (Eq (1)).

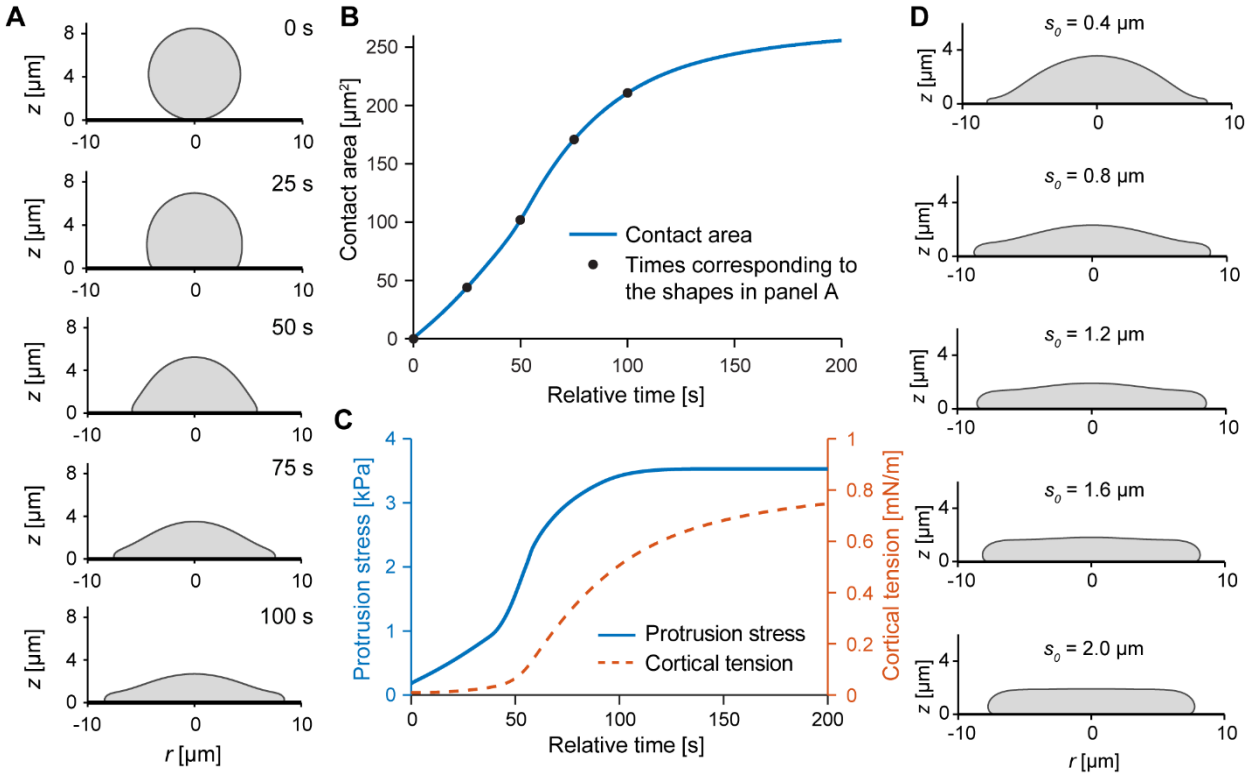

Fig 5. Predictions of the protrusive zipper model in the absence of adhesion stress. (A) For purely protrusion-driven spreading, lamellar pseudopods form as the protrusion stress increases over time. Time stamps of the the shown sample shapes are included. (B) Contact area

404 increases sigmoidally over time for the protrusive zipper model, in good agreement with our
405 measurements of the time course of the mean contact area on the highest density of IgG. Filled
406 circles indicate where the shapes shown in panel A were computed. (C) Protrusion stress
407 (governed by Eq (11)) and cortical tension (governed by Eq (1)) increase during cell spreading.
408 (D) Varying the parameter s_0 determines the thickness of the leading lamella, resulting in a thin
409 pseudopod for s_0 = 0.4 μm (top) and coordinated global cell deformation for s_0 = 2.0 μm
410 (bottom). The sample shapes are shown at t = 120 s. All other protrusive zipper simulations in
411 this paper were carried out using s_0 = 0.8 μm.

412

413 We chose the value s_0 = 0.8 μm for the characteristic length that defines the spatial range
414 of the protrusion stress (Eq (8)) in the simulations shown in Fig 5A-C. Because s_0 does not
415 appear to be a directly measurable quantity, it is instructive to inspect how its value affects the
416 spreading model cell. Snapshots from simulations using different values of s_0 demonstrate how
417 the cell morphology (here: at 120 s) depends on the spatial range over which the protrusion stress
418 acts (Fig 5D, S3 Movie). The leading edge of the cell assumes the shape of a thin lamella for
419 small values of s_0 and becomes increasingly thicker at larger s_0-values. Aside from this varying
420 thickness of cellular protrusions, the overall spreading behavior is similar for different values of
421 s_0.

422 Next, we inspected the behavior of the full protrusive zipper model by repeating the
423 simulation with the same settings as used for Fig 5 but now also including the adhesion stress
424 that captures the contribution of pre-contact attraction between cell and substrate to cell
425 spreading. We again examined the same set of adhesion strengths as used in our tests of the
426 Brownian zipper model (Fig 3). The simulations expose how, in this scenario, cell-substrate
427 adhesion promotes spreading, affecting the overall spreading behavior in a quantitative manner
428 but without altering it qualitatively. The model cells spread somewhat faster and farther on
429 substrates coated with higher ligand densities (Fig 6A), with slightly larger contact angles
430 between their leading edge and the substrate (Fig 6B, S4 Movie), but otherwise exhibited

431 unchanged morphology. The sigmoidal character of the contact-area-versus-time curves is
432 conserved through most of the tested adhesion strengths, and both the spreading speeds as well
433 as the maximum contact areas vary much less than in the predictions of the Brownian zipper
434 model (Fig 3).

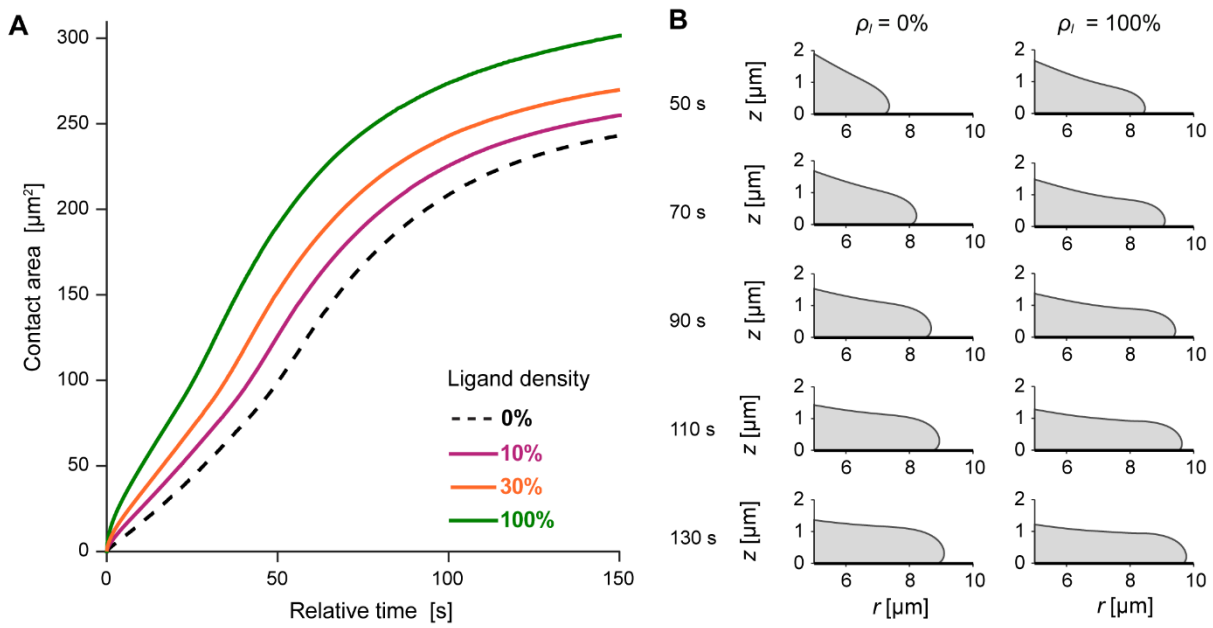

435

436 **Fig 6. Predictions of the protrusive zipper model with varying adhesion stress.**
437 (A) Contact area increases faster and reaches higher values for higher ligand densities. The
438 protrusion-only curve is shown for reference as a dashed line. (B) Magnified views of the leading
439 edge of the model cell highlight subtle, adhesion-dependent changes of the pseudopod
440 morphology. The shapes of the leading cell edge are shown for $\rho_l = 0\%$ and $\rho_l = 100\%$ at times
441 ranging from 50 s to 130 s. On higher ligand density, both the extent of spreading and the
442 dynamic contact angle increase. Other than that, the cell shapes exhibit little dependence on
443 adhesion strength within the full protrusive zipper model.

444

445 Clearly, the predictions of the protrusive zipper model are in much better agreement with
446 experimental observations than those of the Brownian zipper. A spreading cell morphology that
447 is characterized by a forward-bulging leading lamella (Figs. 5-6) matches the cross-sectional
448 profile of phagocytes engulfing large particles well [22, 25], in contrast to model cell shapes

449 whose leading edge coincides with the perimeter of contact between the cell and substrate (Fig
450 3). The timing of spreading and sigmoidal shapes of the contact-area-versus-time curves
451 predicted by the protrusive zipper model (Fig 5-6) agree with experiments as well, and the time-
452 dependent increase in protrusion stress is consistent with a biphasic signaling response measured
453 during FcγR-mediated phagocytosis [42]. Furthermore, both the predicted spreading speeds as
454 well as the maximum contact areas are comparable to the respective values measured in
455 experiments, and the slight increase of the maximum contact area at higher adhesion strengths is
456 consistent with our measurements (Fig 6A). On the other hand, the predicted increase of the
457 spreading speeds on higher ligand densities (Fig 6A) differs from our experimental data (Fig 2).
458 Therefore, this model still somewhat overestimates the contribution of the adhesion stress to the
459 dynamics of phagocytic spreading. Nevertheless, of the two considered models only the
460 protrusive zipper model succeeds in capturing the essential dynamics of experimentally observed
461 phagocytic spreading, establishing that active cellular protrusion rather than passive cell-
462 substrate adhesion is the dominating driving force of this type of cellular motion.

463

464 Protrusive zipper model with discrete adhesion sites: best match
465 between experiments and theory

466 The previous sections presented continuum models of cell spreading, resulting in
467 predictions that overestimated the attractive force due to cell-substrate adhesion even in the case
468 where short-range adhesion plays only a secondary role. In reality, however, adhesive ligands
469 encountered by a spreading cell reside at discrete substrate locations rather than presenting a
470 contiguous adhesive film. A pioneering study that considered discrete adhesion sites not only

predicted dramatic qualitative differences compared to continuum models of adhesion but even concluded that, depending on the lateral spacing of discrete cell-substrate cross-bridges, "there is little or no tendency for the contact to spread unless the surfaces are forced together" [43]. These considerations prompted us to design and examine a version of the protrusive zipper model in which the model cell can only form new attachments to the substrate at prescribed locations (Fig 7, S5 Movie).

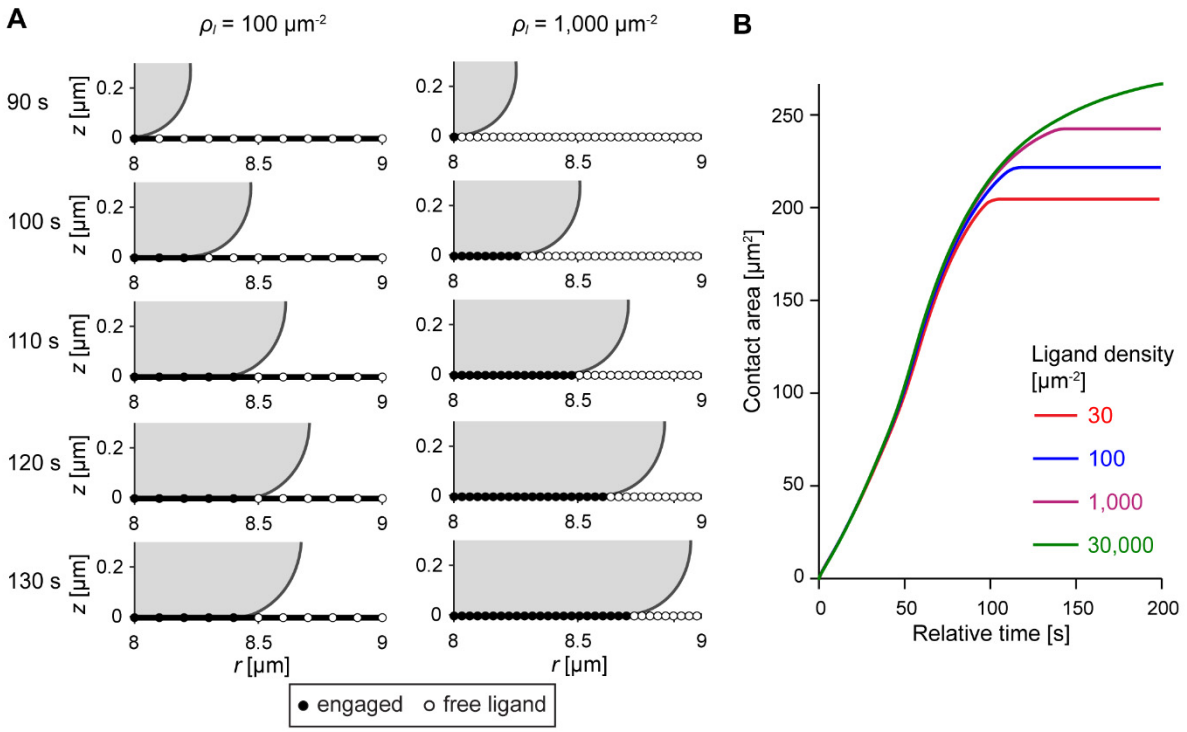

Fig 7. Predictions of the protrusive zipper model with discrete adhesion sites. (A) Two time series (times shown at the left) of simulation snapshots illustrate how the progression of the model cell's leading edge is affected by the spacing of discrete adhesion sites. Unoccupied binding sites are depicted by empty circles, whereas filled circles indicate that the cell membrane is locally attached. (B) Contact-area-versus-time curves share similar slopes over three orders of magnitude of ligand density, but plateau at different maximum contact areas.

In this model version, the spacing of adhesion sites is determined by the ligand density ρ_l (the number of ligand molecules per μm^2), with the in-plane spacing given by $(\rho_l)^{-1/2}$.

487 Furthermore, we introduce two additional rules to capture realistic aspects of cell spreading on
488 discrete adhesion sites. First, we replace the continuous adhesion stress (Eq (6)) with the
489 following concept of discrete bond formation. We consider a new bond as "formed" as soon as
490 the distance between the next free ligand site and the closest point of the advancing cell
491 membrane reaches a threshold distance d_{thresh}. As a consequence of such bonding, we place the
492 cell surface into irreversible contact with this substrate site when carrying out computations at
493 the next time step. The value of the threshold distance is determined by the magnitude of
494 membrane fluctuations. Assuming that the time scale of membrane fluctuations is generally
495 smaller than our time step, we define d_{thresh} to be the root mean square height $<h^2>^{1/2}$ of
496 membrane fluctuations at equilibrium through [44]:

497 $$d_{thresh} = \sqrt{\langle h^2 \rangle} = \sqrt{\frac{k_B T}{4\pi\tau} \ln\left(1 + \frac{\tau A_{cell}}{\pi^2 \kappa_b}\right)} \quad (12)$$

498 where k_B is Boltzmann's constant, T is temperature, A_{cell} is the cell surface area, and κ_b is
499 the membrane bending modulus. According to this rule, increased cortical tension τ suppresses
500 membrane fluctuations, making it more difficult for the cell to form new adhesive connections at
501 later time points. The parameter values chosen in our simulations (S7 Table) correspond to
502 typical fluctuation amplitudes ranging from 18 nm at resting tension to about 2 nm for very high
503 tension, in general agreement with measurements of membrane fluctuations in cells on surfaces
504 [45, 46].

505 Second, because it seems unlikely that persistent receptor-ligand contacts induce
506 signaling indefinitely, we also assume that the protrusion stress can diminish over time. This
507 assumption is supported by experimental data showing that actin polymerization does not
508 continue indefinitely during phagocytosis if the cell encounters an unopsonized region of the

target particle [23, 47, 48]. We implement this behavior by postulating a transient protrusion stress that initially is triggered by fresh cell-substrate contact (occurring at time t_{bind}) and then decays exponentially according to the relation:

$$\tilde{\sigma}_{prot} = \sigma_{prot} e^{-\frac{t - t_{bind}}{t_0}} \tag{13}$$

In this version of the model, σ_{prot} in Eq (8) is replaced by $\tilde{\sigma}_{prot}$ defined in Eq (13). The effects of varying the rate of this decay are explored in S6 Appendices, Appendix F. We use a value of $t_0 = 66$ s in our simulations, which gave the best quantitative agreement with experimental data.

To avoid possible bias due to the exact placement of discrete binding sites, we performed each simulation multiple times, shifting all binding sites laterally by small increments without changing their spacing. We then averaged the results of these individual simulations to predict the cell-spreading behavior as a function of the chosen spacing—or density—of adhesion sites.

Overall, the predictions of this discrete protrusive zipper model (Fig 7) agree well with those of the continuum model version. For instance, maximum cell-substrate contact areas exhibit a similar dependence on the ligand density in both models. However, in this discrete model, the sigmoidal contact-area-versus-time curves obtained at different ligand densities are aligned much more closely during the spreading phase, reflecting spreading speeds that hardly depend on the ligand density anymore (Fig 7B).

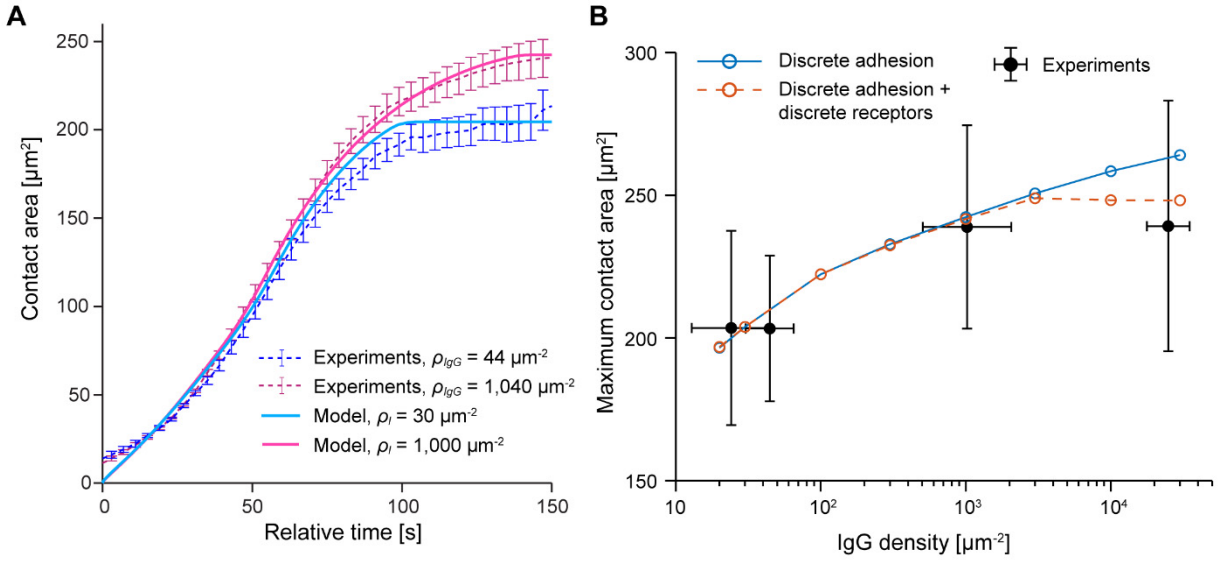

Fig 8. Direct comparison of experimental data with the predictions of the protrusive zipper model with discrete adhesion.
(A) Time courses of the cell-substrate contact area predicted by the protrusive zipper model with discrete adhesion are overlaid on experimental results for two different ligand densities. The model curves are not the result of nonlinear fits but simply the predictions based on reasonable choices of parameter values. (B) The predicted ligand-density-dependent increase in maximum contact area agrees well with experimental results obtained in frustrated phagocytosis experiments. Modeling only ligands as discrete entities results in an apparent overestimation of the maximum contact area at the highest IgG density (*solid blue curve*), indicating that the number of Fcγ receptors rather than the number of IgG ligands becomes the limiting factor of the maximum adhesion strength in this regime. A model version that accounts for the discrete nature of both ligands as well as receptors (S6 Appendices, Appendix F) improves the agreement with the data at the highest IgG density (*dashed red curve*). Error bars indicate standard deviation.

Together, the predictions by the model with discrete adhesion sites agree well with the behavior of real human neutrophils during frustrated phagocytosis (Fig. 8). As in experiments, the spreading speed remains remarkably consistent over a range of ligand densities spanning 3 orders of magnitude (Figs 7B and 8A). Moreover, the predicted moderate increase of the maximum contact area at higher ligand densities matches experimental measurements quite well (Fig 8B). On the other hand, whereas the measured dependence of the maximum contact area on

547 the IgG density appears to reach a plateau for IgG densities greater than 1,000 μm^{-2}, our model
548 predicts a continuous increase of the maximum contact area over the whole range of ligand
549 densities. A possible explanation for this discrepancy is the model assumption that the ligand
550 density determines the maximum number of discrete adhesion bonds between the cell and the
551 substrate, which implies that the receptors on the cell surface are always in excess. Human
552 neutrophils indeed present a large number of Fcγ receptors on their surface, i.e., several thousand
553 receptors per square micrometer. However, this receptor density is smaller than the highest
554 ligand density of ~25,000 IgG molecules per square micrometer used in our experiments.
555 Therefore, at the highest IgG densities, we expect the numbers of receptors to be the limiting
556 factor determining the maximum number of adhesion sites, which is not accounted for in the
557 above model. To verify this expectation, we conducted additional proof-of-principle simulations
558 in which both the ligands as well as the receptors were treated as discrete, as explained in S6
559 Appendices, Appendix F. This approach indeed improved the agreement between experiments
560 and theory further, as shown in Fig. 8B.

561 Overall, these results reinforce the conclusion that active cytoskeletal protrusion drives
562 phagocytic spreading. They also highlight that it can be important for realistic models of cell
563 spreading on substrates coated with specific adhesion molecules to account for the discrete
564 distribution of these adhesion sites.

565

566 # Discussion

567 Quantitative understanding of the behavior of motile mammalian cells—from immune
568 cells to metastasizing cancer cells—is a prerequisite for transformative biomedical advances in

569 diagnosis, treatment, and therapy of many current and future health threats [49]. Motile cells
570 integrate a complex variety of physical and chemical cues to carry out specific functions.
571 Genuine understanding of the underlying mechano-chemical processes not only requires an
572 interdisciplinary strategy but also integrative experimental/theoretical approaches. Translation of
573 mechanistic notions into mathematical models, and comparison of theoretical predictions with
574 experimental observations, often provides the strongest arguments for or against the validity of
575 biological hypotheses. Confidence in the predictive power of computer simulations requires that
576 the model assumptions be realistic and biologically plausible. Guided by this perspective, we
577 here examined fundamental biophysical mechanisms that potentially can facilitate spreading of
578 biological cells on a substrate.

579 Unpolarized cells usually begin spreading in a symmetric fashion [8, 50]. This stage is
580 often viewed as a passive process that is entirely driven by adhesion energy due to receptor-
581 ligand binding [8, 51]. An alternative class of models considers such spreading as dependent on
582 cytoskeletal activity [10, 14, 15]. In this study, we have developed a mechanical modeling
583 framework that allows us to establish whether frustrated phagocytosis, a specific form of
584 isotropic cell spreading, is primarily driven by adhesion (Brownian zipper model) or by
585 protrusive forces generated by the cell (protrusive zipper model). Our findings likely carry over
586 to other types of cell spreading inasmuch as key characteristics of adhesion and protrusion are
587 shared [52].

588 Our results invite a careful review of mathematical models of phagocytosis or other types
589 of cell spreading that consider pre-contact adhesive attraction between cell and substrate as the
590 main driving force [8, 13, 26]. A first important prerequisite for the validity of such models is the
591 use of realistic values of basic mechanical parameters, such as the effective viscosity of the cell

592 interior, the cortical tension, and the adhesion energy density. For example, if the equilibrium
593 cell-substrate contact areas measured in our spreading experiments on low-to-moderate ligand
594 densities were due to adhesion, then the involved adhesion energies would have to be several
595 orders of magnitude higher than those estimated from our measurements of ligand density. Even
596 receptor accumulation in the contact region could not make up for this difference, because the
597 smaller number of available ligands limits the number of possible adhesion bonds. Furthermore,
598 the ability to simulate not only equilibrium situations but also the dynamical cell behavior, and to
599 leverage time-dependent experimental observations against the predictions of such models,
600 considerably raises confidence in a model's evaluation. As demonstrated in this study, such
601 comparison greatly benefits from the availability of experimental data obtained on substrates
602 presenting a large range of known densities of adhesive ligands.

603 It appears that adhesion-driven spreading is largely limited to situations where adhesion
604 is unusually strong, and where the cells—like red blood cells—or surrogate objects—like lipid
605 vesicles—are characterized by a low-viscosity interior and very low tension of their cortex or
606 membrane. Indeed, a recent mechanical modeling study found that Brownian membrane
607 fluctuations were only sufficient to drive very small amounts of cell spreading on a surface [53].
608 If there are cases in which motile mammalian cells spread predominantly due to adhesion, then
609 such spreading will likely occur on much longer timescales than considered here. Finally, it may
610 be possible that adhesion plays a more relevant role in the engulfment of very small particles, or
611 very early during phagocytic spreading, where cell shape changes do not require a significant
612 expansion of the cell surface area [54]. Irrespective of the relevance of Brownian-zipper-type
613 models in a particular practical situation, we note that the excellent agreement of our theoretical

614 treatment of purely adhesion-driven spreading with other studies focusing on this form of motion
615 [8, 13] strengthens confidence in our modeling approach and its numerical implementation.

616 The only alternative mechanism by which cells can expand their region of contact with a
617 suitable substrate appears to be active, protrusion-dominated spreading. Many imaging studies
618 indeed have documented an increased density of F-actin at the protruding front of motile immune
619 cells [16, 55, 56], supporting the biological plausibility of the protrusive zipper concept.
620 Moreover, inhibition of actin polymerization with cytochalasin B or latrunculin A eliminates the
621 rapid phase of fibroblast spreading [10, 14, 57]. Similarly, chemical disruption of the actin
622 cytoskeleton generally inhibits phagocytosis by immune cells [36, 47]. We have previously
623 shown that extremely small concentrations of actin inhibitors actually can increase the size of
624 transient, chemotactic-like protrusions [36, 58]. However, the cortical tension was reduced in
625 such cases, and phagocytic spreading was not enhanced, highlighting the multiplicity of—likely
626 dichotomous—mechanical roles of F-actin during cell deformations.

627 Our simulations based on the protrusive zipper model not only reproduce the main
628 features of neutrophil spreading on IgG-coated substrates but, in the case of discrete adhesion
629 sites, they also agree very well with experimental data. We note that this agreement neither is
630 surprising, nor does it constitute solid proof of the validity of this model. The scarcity of
631 quantitative insights into the underlying mechanisms simply does not place sufficient constraints
632 on the design of computational models. Instead, our goal here was to explore what set of
633 minimalistic rules would need to be postulated to achieve a good match between theory and
634 experiment. The successful implementation of this approach allows us to propose likely
635 mechanistic details that can then provide guidance for future studies. Still, we are confident that
636 the protrusive zipper model paints a reasonably accurate picture of phagocytic spreading, not

637 only because of the elimination of the only alternative hypothesis, but also because our
638 semiempirical model is plausible, i.e., it does not contradict pertinent biophysical and biological
639 insights. For example, our implementation of the relationship between receptor-induced
640 signaling and the generation of protrusive force is consistent with a successful previous model of
641 phagocytosis [22], as well as with previous measurements of the biphasic signaling response
642 from a macrophage-like cell line during Fcγ receptor-mediated phagocytosis [42]. Models based
643 on the assumption that actin polymerization preferentially occurs in regions of higher membrane
644 curvature [59] can result in a localization of protrusion stress that is similar to the form it takes in
645 our model (Fig 1D), although the idea of curvature-induced actin polymerization seems
646 problematic in view of the much higher membrane curvatures in ever-present surface wrinkles
647 and microvilli of immune cells. Importantly, our implementation of the relationship between
648 receptor-induced signaling and force generation is independent of the exact mechanism by which
649 intracellular processes are translated into protrusive force; instead, it encompasses different
650 mechanistic notions such as the Brownian ratchet [60] and end-tracking motors [61].

651 An important outcome of our simulations of the protrusive zipper model is the difference
652 in predictions depending on whether we considered continuous or discrete cell-substrate
653 adhesion, in agreement with a previous theoretical study [43]. We are unaware of physiological
654 situations in which cell adhesion is not predominantly supported by specific receptor-ligand
655 bonds. Thus, the model version that is based on discrete binding sites is the more realistic version
656 of the protrusive zipper. Remarkably, it is also the version that yielded the best match between
657 theory and experimental observations. To achieve this agreement, we postulated that the
658 formation of new receptor-ligand bonds is coupled to the protrusion stress in a time-dependent
659 manner (Eq (13)), based on the assumption that receptor-induced signaling and subsequential

660 actin polymerization are not sustained indefinitely after a ligand activates the receptor. There are
661 multiple factors that could lead to this effective decay, such as the depletion of precursor
662 molecules needed for the production of signaling messengers (e.g. release of IP_3 will cease once
663 PIP_2 has been locally depleted [62]).

664 Perhaps the most important insight from the comparison of model versions based on
665 continuous versus discrete adhesion is that models based on continuous adhesion are likely to
666 misrepresent key aspects of the cell behavior, especially on lower ligand densities. For example,
667 such models cannot capture the possibility that too large ligand spacing may prevent the next
668 unbound receptor-ligand pair from approaching one another to within the distance at which they
669 are likely to form a bond. In our protrusive zipper model with discrete adhesion, variation of
670 substrate adhesivity by changing the density of adhesion sites primarily affects the maximum
671 cell-substrate contact area. This prediction agrees well with our experiments, unlike the
672 predictions by model versions that treat the ligand layer as a continuum.

673 The mechanisms governing isotropic cell spreading studied here are likely to also play a
674 crucial role in the directional motion of migrating cells. Many immune cells, for example, are
675 capable of executing both types of motion, as required during phagocytic spreading versus
676 chemotactic and other forms of migration. As revealed by our experiments and reproduced by
677 our discrete adhesion model, the rate of isotropic cell spreading is largely conserved on
678 substrates presenting a broad range of densities of adhesion sites. This finding exposes an
679 interesting difference to the prediction by models of migrating cells, i.e., that the crawling speed
680 of such cells has a maximum on substrates with intermediate adhesion strengths [63-65]. This
681 difference is a reminder that directional migration generally is a more complex type of motion
682 that involves, in addition to protrusion and adhesion, important mechanisms regulating

contraction and detachment of the rear of the migrating cell from the substrate. The positive correlation between low-to-moderate ligand densities and the speed of motion predicted by models of migrating cells can be attributed to either a direct scaling of protrusion with the amount of adhesion [64], or a postulated increased actin retrograde flow at lower adhesion strengths [63]. The predicted slowing of migrating cells at higher ligand densities is caused by an effective frictional force due to the need to break stronger adhesive attachments at the cell's rear [66, 67]. A noteworthy recent model of cell migration that decoupled friction from adhesive attraction actually predicted faster movement for higher adhesion energies [51]. The excellent agreement between our experiments and the protrusive zipper model suggests that the above additional mechanisms included in models of migrating cells play at most a minor role in isotropic phagocytic spreading. On the other hand, we believe that the main insights exposed by our study provide important suggestions on how to treat the interplay between protrusion and adhesion in models of migrating cells.

Methods

The perturbed Stokes equations

Assuming the cell interior can be approximated by a single, highly viscous, slow-moving Newtonian fluid, its motion obeys the Stokes equations for creeping flow with no body force, as given by Eq (2). Furthermore, for an incompressible fluid, the equation of continuity simplifies to the incompressibility condition (Eq (3)). Due to axial symmetry, there are three unknowns: v_r, v_z, and p, where r and z are cylindrical polar coordinates.

To solve this system of partial differential equations, we use the finite element method (FEM). Because directly solving the Stokes equations using FEM leads to numerical instabilities [68], we follow the procedure outlined by Drury and Dembo [37] to solve a perturbed form of the Stokes equations, in which the incompressibility condition (Eq (3)) is approximated as

$$\nabla \cdot (\mathbf{v} - \epsilon \nabla p) = 0 \tag{14}$$

In this form, the fluid is nearly incompressible, which allows us to avoid the well-known problems with using FEM for incompressible problems [68]. To accurately solve the Stokes equations, the value for ϵ must be sufficiently small. Specifically, we use the condition given in [37]:

$$\epsilon \leq \frac{h_{mesh}^2}{\mu} \tag{15}$$

where h_{mesh} is the characteristic radius of a single quadrilateral element. We tested different values of ϵ in our models and found this condition to provide sufficient accuracy and convergence (S6 Appendices, Appendix E).

Over the unbound portion of the cell, we specify Neumann boundary conditions, corresponding to a stress balance (Eq (4)). For the adherent cell surface, we specify Dirichlet boundary conditions, simply a no-slip condition in this case (Eq (9)). The pressure boundary condition is given by assuming the normal component of the pressure gradient goes to zero at the cell surface:

$$\nabla p \cdot \mathbf{n} = 0 \tag{16}$$

Computational details

At each time step, we first compute values for the surface curvature of the cell. Local values of the angle of the normal ϕ are evaluated using cubic polynomial fits. We then calculate the boundary stresses using the relationships outlined in the main text. The integral for the effective adhesion stress (Eq (6)) is computed numerically as described in S6 Appendices. The values for tension and protrusion stress at each time step are evaluated using smoothed versions of the relationships given in Eq (1) and Eq (11) (see S6 Appendices, Appendix C for full forms).

To find the fluid velocity and pressure fields, we must simultaneously solve Eq (2) and Eq (14) for v_r, v_z, and p. We employ the strategy outlined in [37], which is an adaptation of the Uzawa method. Starting with an estimate for pressure p_{est} given either by the previous time step or as a uniform distribution prior to spreading, we solve for fluid velocities by treating the pressure as known in Eq (2):

$$\mu \nabla^2 \mathbf{v} = \nabla p_{est} \tag{17}$$

We then treat the fluid velocities as known ($\mathbf{v}_{est}$) and solve an altered version of equation (14):

$$\frac{1}{\mu}(p - p_{est}) = \nabla \cdot \mathbf{v}_{est} - \nabla \cdot (\epsilon \nabla p) \tag{18}$$

The updated pressure is then inserted back into Eq (17) and the procedure is repeated until the following condition is met:

$$\frac{\max\left(\left|p - p_{est}\right|\right)}{\max\left(\left|p - p_{out}\right|\right)} \leq 10^{-6} \tag{19}$$

This generally occurs in less than 50 iterations.

The new cell boundary is then given by

$$r(t+\Delta t) = r(t) + v_r \Delta t$$
$$z(t+\Delta t) = z(t) + v_z \Delta t \tag{20}$$

The value for Δt was set relative to the Courant number for each iteration, such that fluid flow occurs over at most 10% of any individual element (S6 Appendices). In the continuum adhesion case (no discrete adhesion sites), the contact line is updated at each time step by computing the intersection between the cell boundary and the surface, then adding all points advected to $z \leq 0$ to the Dirichlet boundary condition (contact, no-slip) for the next time step. In the discrete adhesion model, contact is determined by the distance threshold computed from Eq (12). The contour is smoothed after each advection, and then small corrections are made to the cell contour to compensate for any deviations from constant volume due to smoothing and numerical error.

This model was implemented in MATLAB R2020b (MathWorks) and the full code is available at https://github.com/emmetfrancis/phagocyticSpreading. Individual simulations generally run within 1-3 hours on a personal computer.

Acknowledgements

We thank Dr. Robert Guy from UC Davis Mathematics for many helpful conversations on various iterations of our model and for assistance with the derivation found in S6 Appendices, Appendix B. We also thank Dr. Marc Herant for fruitful discussions on computational modeling of motile cells and Dr. Vasilios Morikis for his feedback on early versions of this manuscript.

References

764 1. Henry SJ, Crocker JC, Hammer DA. Ligand density elicits a phenotypic switch in human
765 neutrophils. Integr Biol (Camb). 2014;6(3):348-56. Epub 2014/02/01. doi: 10.1039/c3ib40225h.
766 PubMed PMID: 24480897; PubMed Central PMCID: PMCPMC5850933.
767 2. Hoang AN, Jones CN, Dimisko L, Hamza B, Martel J, Kojic N, et al. Measuring
768 neutrophil speed and directionality during chemotaxis, directly from a droplet of whole blood.
769 Technology (Singap World Sci). 2013;1(1):49. Epub 2014/05/09. doi:
770 10.1142/S2339547813500040. PubMed PMID: 24809064; PubMed Central PMCID:
771 PMCPMC4010229.
772 3. Ascione F, Vasaturo A, Caserta S, D'Esposito V, Formisano P, Guido S. Comparison
773 between fibroblast wound healing and cell random migration assays in vitro. Exp Cell Res.
774 2016;347(1):123-32. doi: 10.1016/j.yexcr.2016.07.015. PubMed PMID:
775 WOS:000383217500013.
776 4. Czirok A. Endothelial cell motility, coordination and pattern formation during
777 vasculogenesis. Wiley Interdiscip Rev Syst Biol Med. 2013;5(5):587-602. Epub 2013/07/17. doi:
778 10.1002/wsbm.1233. PubMed PMID: 23857825; PubMed Central PMCID: PMCPMC3737767.
779 5. Schneider L, Cammer M, Lehman J, Nielsen SK, Guerra CF, Veland IR, et al.
780 Directional cell migration and chemotaxis in wound healing response to PDGF-AA are
781 coordinated by the primary cilium in fibroblasts. Cell Physiol Biochem. 2010;25(2-3):279-92.
782 Epub 2010/01/30. doi: 10.1159/000276562. PubMed PMID: 20110689; PubMed Central
783 PMCID: PMCPMC2924811.
784 6. Morrissey MA, Williamson AP, Steinbach AM, Roberts EW, Kern N, Headley MB, et al.
785 Chimeric antigen receptors that trigger phagocytosis. Elife. 2018;7. doi: ARTN e36688
786 10.7554/eLife.36688. PubMed PMID: WOS:000435593500001.

787 7. Feng MY, Jiang W, Kim BYS, Zhang CC, Fu YX, Weissman IL. Phagocytosis
788 checkpoints as new targets for cancer immunotherapy. Nat Rev Cancer. 2019;19(10):568-86.
789 doi: 10.1038/s41568-019-0183-z. PubMed PMID: WOS:000492743400012.
790 8. Cuvelier D, Thery M, Chu YS, Dufour S, Thiery JP, Bornens M, et al. The universal
791 dynamics of cell spreading. Curr Biol. 2007;17(8):694-9. Epub 2007/03/24. doi:
792 10.1016/j.cub.2007.02.058. PubMed PMID: 17379524.
793 9. Dubin-Thaler BJ, Giannone G, Dobereiner HG, Sheetz MP. Nanometer analysis of cell
794 spreading on matrix-coated surfaces reveals two distinct cell states and STEPs. Biophys J.
795 2004;86(3):1794-806. Epub 2004/03/03. doi: 10.1016/S0006-3495(04)74246-0. PubMed PMID:
796 14990505; PubMed Central PMCID: PMCPMC1304013.
797 10. Xiong Y, Rangamani P, Fardin MA, Lipshtat A, Dubin-Thaler B, Rossier O, et al.
798 Mechanisms controlling cell size and shape during isotropic cell spreading. Biophys J.
799 2010;98(10):2136-46. Epub 2010/05/21. doi: 10.1016/j.bpj.2010.01.059. PubMed PMID:
800 20483321; PubMed Central PMCID: PMCPMC2872297.
801 11. Reinhart-King CA, Dembo M, Hammer DA. The dynamics and mechanics of endothelial
802 cell spreading. Biophys J. 2005;89(1):676-89. Epub 2005/04/26. doi:
803 10.1529/biophysj.104.054320. PubMed PMID: 15849250; PubMed Central PMCID:
804 PMCPMC1366566.
805 12. Carter SB. Haptotaxis and the mechanism of cell motility. Nature. 1967;213(5073):256-
806 60. Epub 1967/01/21. doi: 10.1038/213256a0. PubMed PMID: 6030602.
807 13. Etienne J, Duperray A. Initial dynamics of cell spreading are governed by dissipation in
808 the actin cortex. Biophys J. 2011;101(3):611-21. Epub 2011/08/03. doi:

809 10.1016/j.bpj.2011.06.030. PubMed PMID: 21806929; PubMed Central PMCID:
810 PMCPMC3145312.
811 14. Fardin MA, Rossier OM, Rangamani P, Avigan PD, Gauthier NC, Vonnegut W, et al.
812 Cell spreading as a hydrodynamic process. Soft Matter. 2010;6(19):4788-99. doi:
813 10.1039/c0sm00252f. PubMed PMID: WOS:000282008300022.
814 15. Herant M, Dembo M. An integrative toy model of cell flattening, spreading, and ruffling.
815 Biorheology. 2015;52(5-6):405-14. Epub 2015/11/26. doi: 10.3233/BIR-14042. PubMed PMID:
816 26600264.
817 16. Kovari DT, Wei W, Chang P, Toro JS, Beach RF, Chambers D, et al. Frustrated
818 Phagocytic Spreading of J774A-1 Macrophages Ends in Myosin II-Dependent Contraction.
819 Biophys J. 2016;111(12):2698-710. Epub 2016/12/22. doi: 10.1016/j.bpj.2016.11.009. PubMed
820 PMID: 28002746; PubMed Central PMCID: PMCPMC5194617.
821 17. Cannon GJ, Swanson JA. The macrophage capacity for phagocytosis. J Cell Sci.
822 1992;101 (Pt 4):907-13. Epub 1992/04/01. PubMed PMID: 1527185.
823 18. Champion JA, Mitragotri S. Role of target geometry in phagocytosis. Proc Natl Acad Sci
824 U S A. 2006;103(13):4930-4. Epub 2006/03/22. doi: 10.1073/pnas.0600997103. PubMed PMID:
825 16549762; PubMed Central PMCID: PMCPMC1458772.
826 19. Callens SJP, Uyttendaele RJC, Fratila-Apachitei LE, Zadpoor AA. Substrate curvature as
827 a cue to guide spatiotemporal cell and tissue organization. Biomaterials. 2020;232:119739. Epub
828 2020/01/09. doi: 10.1016/j.biomaterials.2019.119739. PubMed PMID: 31911284.
829 20. van der Putten C, Buskermolen ABC, Werner M, Brouwer HFM, Bartels PAA, Dankers
830 PYW, et al. Protein Micropatterning in 2.5D: An Approach to Investigate Cellular Responses in
831 Multi-Cue Environments. ACS Appl Mater Interfaces. 2021;13(22):25589-98. Epub 2021/05/26.

832 doi: 10.1021/acsami.1c01984. PubMed PMID: 34032413; PubMed Central PMCID:
833 PMCPMC8193632.
834 21. Richards DM, Endres RG. Target shape dependence in a simple model of receptor-
835 mediated endocytosis and phagocytosis. Proc Natl Acad Sci U S A. 2016;113(22):6113-8. Epub
836 2016/05/18. doi: 10.1073/pnas.1521974113. PubMed PMID: 27185939; PubMed Central
837 PMCID: PMCPMC4896703.
838 22. Herant M, Heinrich V, Dembo M. Mechanics of neutrophil phagocytosis: experiments
839 and quantitative models. J Cell Sci. 2006;119(Pt 9):1903-13. Epub 2006/04/26. doi:
840 10.1242/jcs.02876. PubMed PMID: 16636075.
841 23. Heinrich V. Controlled One-on-One Encounters between Immune Cells and Microbes
842 Reveal Mechanisms of Phagocytosis. Biophys J. 2015;109(3):469-76. Epub 2015/08/06. doi:
843 10.1016/j.bpj.2015.06.042. PubMed PMID: 26244729; PubMed Central PMCID:
844 PMCPMC4572503.
845 24. Francis EA, Xiao H, Teng LH, Heinrich V. Mechanisms of frustrated phagocytic
846 spreading of human neutrophils on antibody-coated surfaces. BioRxiv [Preprint]. 2022. Epub
847 February 22, 2022. doi: 10.1101/2022.02.18.481104.
848 25. Lee C-Y, Thompson III GR, Hastey CJ, Hodge GC, Lunetta JM, Pappagianis D, et al.
849 *Coccidioides* Endospores and Spherules Draw Strong Chemotactic, Adhesive, and Phagocytic
850 Responses by Individual Human Neutrophils. PLoS ONE. 2015;10(6):e0129522. doi:
851 10.1371/journal.pone.0129522.
852 26. Tollis S, Dart AE, Tzircotis G, Endres RG. The zipper mechanism in phagocytosis:
853 energetic requirements and variability in phagocytic cup shape. BMC Syst Biol. 2010;4:149.

854 Epub 2010/11/10. doi: 10.1186/1752-0509-4-149. PubMed PMID: 21059234; PubMed Central
855 PMCID: PMCPMC2991294.
856 27. Yeung A, Evans E. Cortical shell-liquid core model for passive flow of liquid-like
857 spherical cells into micropipets. Biophys J. 1989;56(1):139-49. Epub 1989/07/01. doi:
858 10.1016/S0006-3495(89)82659-1. PubMed PMID: 2752083; PubMed Central PMCID:
859 PMCPMC1280459.
860 28. Tran-Son-Tay R, Needham D, Yeung A, Hochmuth RM. Time-dependent recovery of
861 passive neutrophils after large deformation. Biophys J. 1991;60(4):856-66. Epub 1991/10/01.
862 doi: 10.1016/S0006-3495(91)82119-1. PubMed PMID: 1742456; PubMed Central PMCID:
863 PMCPMC1260136.
864 29. Manley HR, Keightley MC, Lieschke GJ. The Neutrophil Nucleus: An Important
865 Influence on Neutrophil Migration and Function. Front Immunol. 2018;9:2867. Epub
866 2018/12/20. doi: 10.3389/fimmu.2018.02867. PubMed PMID: 30564248; PubMed Central
867 PMCID: PMCPMC6288403.
868 30. Murphy K, Weaver C. Janeway's immunobiology. 9th edition. ed. New York, NY:
869 Garland Science/Taylor & Francis Group, LLC; 2016. xx, 904 pages p.
870 31. Herant M, Marganski WA, Dembo M. The mechanics of neutrophils: synthetic modeling
871 of three experiments. Biophys J. 2003;84(5):3389-413. Epub 2003/04/30. doi: 10.1016/s0006-
872 3495(03)70062-9. PubMed PMID: 12719267; PubMed Central PMCID: PMCPMC1302898.
873 32. Herant M, Lee CY, Dembo M, Heinrich V. Protrusive push versus enveloping embrace:
874 computational model of phagocytosis predicts key regulatory role of cytoskeletal membrane
875 anchors. PLoS Comput Biol. 2011;7(1):e1001068. doi: 10.1371/journal.pcbi.1001068. PubMed
876 PMID: 21298079; PubMed Central PMCID: PMCPMC3029235.

877 33. Zak A, Merino-Cortes SV, Sadoun A, Mustapha F, Babataheri A, Dogniaux S, et al.
878 Rapid viscoelastic changes are a hallmark of early leukocyte activation. Biophys J. 2021. Epub
879 2021/03/18. doi: 10.1016/j.bpj.2021.02.042. PubMed PMID: 33730552.
880 34. Needham D, Hochmuth RM. A sensitive measure of surface stress in the resting
881 neutrophil. Biophys J. 1992;61(6):1664-70. Epub 1992/06/01. doi: 10.1016/S0006-
882 3495(92)81970-7. PubMed PMID: 1617145; PubMed Central PMCID: PMCPMC1260460.
883 35. Herant M, Heinrich V, Dembo M. Mechanics of neutrophil phagocytosis: behavior of the
884 cortical tension. J Cell Sci. 2005;118(Pt 9):1789-97. Epub 2005/04/14. doi: 10.1242/jcs.02275.
885 PubMed PMID: 15827090.
886 36. Lee CY, Herant M, Heinrich V. Target-specific mechanics of phagocytosis: protrusive
887 neutrophil response to zymosan differs from the uptake of antibody-tagged pathogens. J Cell Sci.
888 2011;124(Pt 7):1106-14. Epub 2011/03/10. doi: 10.1242/jcs.078592. PubMed PMID: 21385838;
889 PubMed Central PMCID: PMCPMC3056606.
890 37. Drury JL, Dembo M. Hydrodynamics of micropipette aspiration. Biophys J. 1999;76(1 Pt
891 1):110-28. Epub 1999/01/06. doi: 10.1016/S0006-3495(99)77183-3. PubMed PMID: 9876128;
892 PubMed Central PMCID: PMCPMC1302505.
893 38. Maenaka K, van der Merwe PA, Stuart DI, Jones EY, Sondermann P. The human low
894 affinity Fcgamma receptors IIa, IIb, and III bind IgG with fast kinetics and distinct
895 thermodynamic properties. J Biol Chem. 2001;276(48):44898-904. Epub 2001/09/07. doi:
896 10.1074/jbc.M106819200. PubMed PMID: 11544262.
897 39. Bonn D, Eggers J, Indekeu J, Meunier J, Rolley E. Wetting and spreading. Rev Mod
898 Phys. 2009;81(2):739-805. doi: 10.1103/RevModPhys.81.739. PubMed PMID:
899 WOS:000267197500008.

900 40. Marcy Y, Prost J, Carlier MF, Sykes C. Forces generated during actin-based propulsion:
901 a direct measurement by micromanipulation. Proc Natl Acad Sci U S A. 2004;101(16):5992-7.
902 Epub 2004/04/14. doi: 10.1073/pnas.0307704101. PubMed PMID: 15079054; PubMed Central
903 PMCID: PMCPMC395911.
904 41. Parekh SH, Chaudhuri O, Theriot JA, Fletcher DA. Loading history determines the
905 velocity of actin-network growth. Nat Cell Biol. 2005;7(12):1219-23. Epub 2005/11/22. doi:
906 10.1038/ncb1336. PubMed PMID: 16299496.
907 42. Zhang Y, Hoppe AD, Swanson JA. Coordination of Fc receptor signaling regulates
908 cellular commitment to phagocytosis. Proc Natl Acad Sci U S A. 2010;107(45):19332-7. Epub
909 2010/10/27. doi: 10.1073/pnas.1008248107. PubMed PMID: 20974965; PubMed Central
910 PMCID: PMCPMC2984174.
911 43. Evans EA. Detailed mechanics of membrane-membrane adhesion and separation. II.
912 Discrete kinetically trapped molecular cross-bridges. Biophys J. 1985;48(1):185-92. Epub
913 1985/07/01. doi: 10.1016/S0006-3495(85)83771-1. PubMed PMID: 4016208; PubMed Central
914 PMCID: PMCPMC1329388.
915 44. Helfrich W, Servuss RM. Undulations, Steric Interaction and Cohesion of Fluid
916 Membranes. Nuovo Cimento D. 1984;3(1):137-51. doi: Doi 10.1007/Bf02452208. PubMed
917 PMID: WOS:A1984SF44800012.
918 45. Biswas A, Alex A, Sinha B. Mapping Cell Membrane Fluctuations Reveals Their Active
919 Regulation and Transient Heterogeneities. Biophys J. 2017;113(8):1768-81. Epub 2017/10/19.
920 doi: 10.1016/j.bpj.2017.08.041. PubMed PMID: 29045871; PubMed Central PMCID:
921 PMCPMC5647594.

922 46. Turlier H, Betz T. Fluctuations in Active Membranes. In: Bassereau P, Sens P, editors.
923 Physics of Biological Membranes. Cham: Springer International Publishing; 2018. p. 581-619.
924 47. van Zon JS, Tzircotis G, Caron E, Howard M. A mechanical bottleneck explains the
925 variation in cup growth during FcgammaR phagocytosis. Mol Syst Biol. 2009;5:298. Epub
926 2009/08/20. doi: 10.1038/msb.2009.59. PubMed PMID: 19690567; PubMed Central PMCID:
927 PMCPMC2736656.
928 48. Griffin FM, Jr., Griffin JA, Leider JE, Silverstein SC. Studies on the mechanism of
929 phagocytosis. I. Requirements for circumferential attachment of particle-bound ligands to
930 specific receptors on the macrophage plasma membrane. J Exp Med. 1975;142(5):1263-82. Epub
931 1975/11/11. doi: 10.1084/jem.142.5.1263. PubMed PMID: 1194852; PubMed Central PMCID:
932 PMCPMC2189973.
933 49. Francis EA, Heinrich V. Mechanistic Understanding of Single-Cell Behavior is Essential
934 for Transformative Advances in Biomedicine. Yale J Biol Med. 2018;91(3):279-89. Epub
935 2018/09/28. PubMed PMID: 30258315; PubMed Central PMCID: PMCPMC6153630.
936 50. McGrath JL. Cell spreading: the power to simplify. Curr Biol. 2007;17(10):R357-8. Epub
937 2007/05/16. doi: 10.1016/j.cub.2007.03.057. PubMed PMID: 17502086.
938 51. Cao Y, Karmakar R, Ghabache E, Gutierrez E, Zhao Y, Groisman A, et al. Cell motility
939 dependence on adhesive wetting. Soft Matter. 2019;15(9):2043-50. Epub 2019/02/07. doi:
940 10.1039/c8sm01832d. PubMed PMID: 30724956.
941 52. Cougoule C, Wiedemann A, Lim J, Caron E. Phagocytosis, an alternative model system
942 for the study of cell adhesion. Semin Cell Dev Biol. 2004;15(6):679-89. Epub 2004/11/25. doi:
943 10.1016/j.semcdb.2004.09.001. PubMed PMID: 15561587.

944 53. DiNapoli KT, Robinson DN, Iglesias PA. A mesoscale mechanical model of cellular
945 interactions. Biophys J. 2021;120(22):4905-17. Epub 2021/10/24. doi:
946 10.1016/j.bpj.2021.10.021. PubMed PMID: 34687718; PubMed Central PMCID:
947 PMCPMC8633826.
948 54. Richards DM, Endres RG. The mechanism of phagocytosis: two stages of engulfment.
949 Biophys J. 2014;107(7):1542-53. Epub 2014/10/09. doi: 10.1016/j.bpj.2014.07.070. PubMed
950 PMID: 25296306; PubMed Central PMCID: PMCPMC4190621.
951 55. Nelsen E, Hobson CM, Kern ME, Hsiao JP, O'Brien Iii ET, Watanabe T, et al. Combined
952 Atomic Force Microscope and Volumetric Light Sheet System for Correlative Force and
953 Fluorescence Mechanobiology Studies. Sci Rep. 2020;10(1):8133. Epub 2020/05/20. doi:
954 10.1038/s41598-020-65205-8. PubMed PMID: 32424215; PubMed Central PMCID:
955 PMCPMC7234992.
956 56. Fritz-Laylin LK, Riel-Mehan M, Chen BC, Lord SJ, Goddard TD, Ferrin TE, et al. Actin-
957 based protrusions of migrating neutrophils are intrinsically lamellar and facilitate direction
958 changes. Elife. 2017;6. Epub 2017/09/28. doi: 10.7554/eLife.26990. PubMed PMID: 28948912;
959 PubMed Central PMCID: PMCPMC5614560.
960 57. Dubin-Thaler BJ, Hofman JM, Cai Y, Xenias H, Spielman I, Shneidman AV, et al.
961 Quantification of cell edge velocities and traction forces reveals distinct motility modules during
962 cell spreading. PLoS One. 2008;3(11):e3735. Epub 2008/11/18. doi:
963 10.1371/journal.pone.0003735. PubMed PMID: 19011687; PubMed Central PMCID:
964 PMCPMC2581916.

965 58. Heinrich V, Lee C-Y. Blurred line between chemotactic chase and phagocytic
966 consumption: an immunophysical single-cell perspective. Journal of Cell Science.
967 2011;124(18):3041-51. doi: 10.1242/jcs.086413.
968 59. Sadhu RK, Penic S, Iglic A, Gov NS. Modelling cellular spreading and emergence of
969 motility in the presence of curved membrane proteins and active cytoskeleton forces. Eur Phys J
970 Plus. 2021;136(5). doi: ARTN 495

971 10.1140/epjp/s13360-021-01433-9. PubMed PMID: WOS:000651515200002.
972 60. Mogilner A, Oster G. Cell motility driven by actin polymerization. Biophys J.
973 1996;71(6):3030-45. Epub 1996/12/01. doi: 10.1016/S0006-3495(96)79496-1. PubMed PMID:
974 8968574; PubMed Central PMCID: PMCPMC1233792.
975 61. Dickinson RB, Caro L, Purich DL. Force generation by cytoskeletal filament end-
976 tracking proteins. Biophys J. 2004;87(4):2838-54. Epub 2004/09/30. doi:
977 10.1529/biophysj.104.045211. PubMed PMID: 15454475; PubMed Central PMCID:
978 PMCPMC1304702.
979 62. Flannagan RS, Jaumouille V, Grinstein S. The cell biology of phagocytosis. Annu Rev
980 Pathol. 2012;7:61-98. Epub 2011/09/14. doi: 10.1146/annurev-pathol-011811-132445. PubMed
981 PMID: 21910624.
982 63. Barnhart EL, Lee KC, Keren K, Mogilner A, Theriot JA. An adhesion-dependent switch
983 between mechanisms that determine motile cell shape. PLoS Biol. 2011;9(5):e1001059. Epub
984 2011/05/12. doi: 10.1371/journal.pbio.1001059. PubMed PMID: 21559321; PubMed Central
985 PMCID: PMCPMC3086868.
986 64. Ziebert F, Aranson IS. Effects of adhesion dynamics and substrate compliance on the
987 shape and motility of crawling cells. PLoS One. 2013;8(5):e64511. Epub 2013/06/07. doi:

988 10.1371/journal.pone.0064511. PubMed PMID: 23741334; PubMed Central PMCID:
989 PMCPMC3669322.
990 65. Copos CA, Walcott S, Del Alamo JC, Bastounis E, Mogilner A, Guy RD.
991 Mechanosensitive Adhesion Explains Stepping Motility in Amoeboid Cells. Biophys J.
992 2017;112(12):2672-82. Epub 2017/06/22. doi: 10.1016/j.bpj.2017.04.033. PubMed PMID:
993 28636923; PubMed Central PMCID: PMCPMC5478966.
994 66. Shao D, Levine H, Rappel WJ. Coupling actin flow, adhesion, and morphology in a
995 computational cell motility model. Proc Natl Acad Sci U S A. 2012;109(18):6851-6. Epub
996 2012/04/12. doi: 10.1073/pnas.1203252109. PubMed PMID: 22493219; PubMed Central
997 PMCID: PMCPMC3344950.
998 67. Kuusela E, Alt W. Continuum model of cell adhesion and migration. J Math Biol.
999 2009;58(1-2):135-61. Epub 2008/05/20. doi: 10.1007/s00285-008-0179-x. PubMed PMID:
1000 18488227.
1001 68. Hughes TJR. The Finite Element Method: Linear Static and Dynamic Finite Element
1002 Analysis: Dover; 2000.

1003

1004 Supporting Information

1005 **S1 Movie. Simulations of purely adhesive cell spreading ("Brownian zipper") on substrates**
1006 **presenting different densities of adhesion sites.** This sequence of animations shows side views
1007 of model cells spreading on adhesive substrates coated with relative ligand densities (ρ_l) of 1%,
1008 3%, 10%, 30%, and 100% for 400 s in the absence of protrusion stress.

1009 **S2 Movie. Simulation of purely protrusion-driven cell spreading.** This animation shows a
1010 side view of a model cell spreading on a flat substrate for 200 s. The cell motion is assumed to be
1011 driven exclusively by active cytoskeletal protrusion at a maximum protrusion stress of $\sigma_{prot,max}$ =
1012 3.5 kPa. Cell-substrate contact, once established, is assumed to be permanent. All other
1013 contributions of adhesive cell-substrate interactions to spreading are neglected.

1014 **S3 Movie. Effect of the range of action of the protrusion stress on purely protrusion-driven**
1015 **cell spreading.** This sequence of simulations shows side views of model cells spreading in the
1016 absence of adhesion stress for 200 s. Increasing the range s_0 over which cytoskeletal protrusion
1017 actively pushes the cellular pseudopod outwards (given in terms of the arc length of the free cell
1018 contour, measured from the point of substrate contact) results in thicker pseudopods. In this
1019 sequence, s_0 = 0.4 μm, 1.2 μm, and 2.0 μm, respectively. In all examples, $\sigma_{prot,max} \times s_0$ = 2.8
1020 mN/m.

1021 **S4 Movie. Minor role of cell-substrate adhesion stress in protrusion-dominated cell**
1022 **spreading ("protrusive zipper").** This sequence of simulations compares magnified views of
1023 purely protrusion-driven spreading (adhesion stress ρ_l = 0%) with protrusion-driven spreading in
1024 the presence of moderate and strong adhesion stress (ρ_l = 10% and 100%, respectively). In all
1025 examples, $\sigma_{prot,max}$ = 3.5 kPa.

1026 **S5 Movie. Protrusive zipper simulations with discrete adhesion sites.** This sequence of
1027 simulations shows a magnified view of protrusion-driven spreading ($\sigma_{prot,max}$ = 3.5 kPa) on
1028 substrates presenting different densities of discrete adhesion sites (ρ_l = 30 μm^{-2}, 100 μm^{-2}, 1,000
1029 μm^{-2}, and 10,000 μm^{-2}). Open circles denote free adhesive binding sites, and filled circles depict
1030 sites with engaged ligand.

S6 Appendices. Derivation of important relationships and summary of numerical testing. (A) Adhesion stress calculation. (B) Derivation of a power law for contact area growth in passive spreading. (C) Development and testing of constitutive relations for cortical tension and protrusion stress. (D) Details of finite element implementation. (E) Summary of numerical testing. (F) Additional testing of the discrete adhesion model.

S7 Table. Summary of modeling parameters, with supporting references.